




Structural, optical, and magnetic properties of iron-doped ZnO nanoparticles for optoelectronics

Ragaa S. Mahmoud¹, A. Abu El-Fadl¹, A. A. Abu-Sehly¹, B. M. Alotaibi², Albandari W. Alrowaily², A. M. Aboaraia^{3,*} , and E. R. Shaaban³

¹ Physics Department, Faculty of Science, Assiut University, Assiut 71516, Egypt

² Department of Physics, College of Science, Princess Nourah Bint Abdulrahman University, P.O. Box 84428, Riyadh 11671, Saudi Arabia

³ Physics Department, Faculty of Science, Al-Azhar University, Assiut 71542, Egypt

Received: 2 July 2022

Accepted: 7 September 2022

Published online:
27 September 2022

© The Author(s), under exclusive licence to Springer Science+Business Media, LLC, part of Springer Nature 2022

ABSTRACT

Pristine ZnO and iron-doped ZnO ($x = 0, 0.04, 0.08, 0.10,$ and 0.15) nanoparticles were produced by means of precipitation route. The nanoparticles were subjected to thermogravimetric analysis. Both EDX and XPS were employed to analyze the chemical structure of samples. The XRD pattern shows that the hexagonal structure of iron-doped ZnO nanoparticles is known, and this suggests that Fe²⁺ can substitute Zn²⁺ in the lattice of ZnO without the discovery of another precipitated phase. As the amount of Fe material increases, the lattice strain rises from 0.0277 to 0.0379, even though a crystallite size falls from 38 to 28 nm, x is equal 0, and 0.15, respectively. The only factors that significantly affect the shrinking of crystallite size are preparation conditions and structural disorder. In terms of UV–vis absorption spectroscopy, the energy gap, E_g^{opt} value obtained from the derivative of absorbance concerning wavelength and found to be reduced from 3.41 eV when x of around 0 and 3.1 eV when x of around 0.15 with rising Fe content. The photoluminescence spectrometry can produce wide PL peaks because of the numerous recombination faults and sites. The presence of additional peaks from an intrinsic emission is thought to be the cause of the PL's asymmetric spectrum. The M-H measurements demonstrated RT ferromagnetism in the Fe-doped ZnO nanoparticles by vibrating the sample in a magnetometer. Additionally, the coercive field increases from 59.9 G to 85.3 G and the remanent magnetization increases from 3.4×10^{-3} to 21×10^{-3} emu/g when the iron content rises from (x of around 0.02) to (x of around 0.15). By improving the magnetic and optical properties of samples, these findings enable the use of iron-doped ZnO nanoparticles in optoelectronic and spintronic applications.

Address correspondence to E-mail: a.m.aboaraia@gmail.com

1 Introduction

Materials called diluted magnetic semiconductors (DMS) are created by replacing the cations of non-magnetic semiconductors with transition metal “TM” ions or rare earth ions [1]. The ferromagnetism detected in strain gauges gets attracted intensive research for its potential application in spintronic devices that exploit the spin and electronic charge of magnetic materials [2]. In addition, doping of transition metals in wide-bandgap semiconductors can also lead to fine adjustment of an optical and ferromagnetic property [3–5]. Fundamental ferromagnetism, including high Curie temperature, is an essential condition for strain gages for spintronic devices [6, 7]. As a result, work is being devoted to fabricating TM metal-doped wide-bandgap semiconductors with RT ferromagnetism (RTFM). ZnO is an II–VI compound semiconductor with a broad bandgap ~ 3.37 eV and large exciton binding energy “60 meV”, with a hexagonal structure with a P63mc space group [8]. The requirement for a Curie temperature (greater than Curie temperature) and intrinsic ferromagnetism (FM) due to the second phase of magnetic collections or in spintronic applications makes transition metal-doped ZnO. Since RTFM-based applications have been observed in several ZnO systems together with Mn, Co, and Fe-doped ZnO [9]. Relatively conflicting results have been reported for ferromagnetism in TM-doped Zinc Oxide. Liu and co-author [9] described RTFM and interpreted it as an inherent property of Iron-doped ZnO. Transition metals have also been found to play no influence on the magnetism of iron and manganese-doped ZnO films [10]. Bhargava and co-author [11] examined ferromagnetism in chromium-doped ZnO, and Taher and co-author [12] studied ferromagnetism in co-doped nanostructured ZnO films, which is practically caused by oxygen vacancies presented in the films through hydrothermal growth. The doping of ZnO by Iron (Fe) reduced the bandgap. The energy gap of the ZnO semiconductor material may be minimized by appropriately altering the stoichiometry ratio of the Fe dopant, and we can obtain a new material with distinct characteristics from their inherent complement. Nano-sized Fe-doped ZnO nanomaterials have gotten a lot of interest in this area.

In iron-doped ZnO nanostructures, create via a chemical rooting and ascribed their origin to zinc

vacancies (Zni) [13], Wei and co-authors studied ferromagnetism in Iron-doped ZnO and ascribed to the second phase at high doping concentration [14]. Despite numerous reports in the literature, there is conflict over the basis of the RTFM noted in transition metal-doped ZnO strain gauges. Some theories show that doping ZnO nanoparticles, including these TMs will result in significant changes in their luminous and magnetic characteristics. Nevertheless, the underlying system of RTFM in iron-doped ZnO is unknown, and the relationship among the magnetic and optical characteristics is not entirely evident due to contradicting results in the works. These contradicting findings imply that RTFM in (DMS) may be especially sensitive to preparatory techniques. This paper purpose of synthesizing high-quality nanoparticle samples from pristine ZnO and Iron-doped ZnO by various concentrations to study the micro-structural parameters, morphology, optical properties, and the effect of Fe doping on the energy gap and magnetic properties of nanoparticles for spintronic applications.

2 Experimental aspects

2.1 Undoped and iron-doped ZnO nanoparticles synthesis

Dissolve $\text{Zn}(\text{NO}_3)_2 \cdot 6\text{H}_2\text{O}$ and a suitable quantity of $\text{Fe}(\text{NO}_3)_3 \cdot 9\text{H}_2\text{O}$ (Sigma-Aldrich Co., USA) to yield the desired doping percentage of $\text{Zn}_{1-x}\text{Fe}_x\text{O}$ ($x = 0, 0.04, 0.08, 0.10$ and 0.15) in 50 mL of distilling water. The zinc nitrate and ferric nitrate were dissolved in Di water to obtain a clear solution, which was then stirred for an additional hour. To the prepared solution, NH_4OH solution was added dropwise until the pH of the solution was ~ 9 . The mix was stirred at room temperature for 3 h and separated by center fusion. The powder precipitate was in the muffle furnace at 80°C for 5 h. The thermal performance of the precursors was examined by TGA (Shimadzu 50 with a precision of ± 0.1 K). Lastly, the dry samples were ground and calcined at 520°C for 2 h to get powder samples.

2.2 Experimental methods

The thermal behavior of the precursors was detected by the (TGA). The structure of ZnO and Fe/ZnO

samples were detected using (XRD) Philips X-ray diffractometer X-mode with Cu-K α 1 radiation. Crystalline silica ($\sim 99.9999\%$) was used as an interior standard. Compositional analysis by (EDX) spectroscopy and XPS “KALPHA device” were used to examine the property of the band structure. Both PL and absorbance spectra were measured using a dual beam spectrophotometer (JASCO 670). To study the magnetism of Zn $_{1-x}$ Fe $_x$ O ($x = 0, 0.04, 0.08, 0.10$ and 0.15), we performed field-dependent magnetization (M-H) measurements in magnetic fields up to 40 KG at RT using a vibrating sample magnetometer (VSM-9600 M-1, USA).

3 Results and discussion

3.1 TG analysis

The thermal treatment is essential to form the single-phase metal oxide after the precipitate is cleaned with DI water and dried at 100 °C. Accordingly, thermal gravimetric analysis (TGA) measurements of Fe-doped ZnO nanoparticles were performed to examine the best possible calcination temperature. Figures 1a, b demonstrates the TG analysis curves of pristine and 10% iron-doped ZnO nanoparticles, carried out with thermal treatment at a rate of 5 °C / min up to 750 °C in air. It is clearly seen that the weight loss reduces with the growth in the temperature ~ 519 °C. In the range of temperature after 519 °C, no remarkable critical variation in the loss of weight was observed; therefore, the suitable calcination temperature is at least over 520 °C. Furthermore, three steps of decompositions have been identified in

the TGA measurements (mass loss). The first step belongs to water decomposition is detected at 0.92% and 0.6% for pristine and 10% iron-doped ZnO samples, correspondingly. The second step corresponds to organic decomposition at 2.6%, and 2.05% for pristine and 10% iron-doped ZnO powder samples, correspondingly.

3.2 Elemental composition analysis

Chemical Compositions analysis of pristine ZnO and iron-doped ZnO nanoparticles were examined by (EDXS). Figure 2 displayed the EDX spectra for pristine ZnO and Zn $_{0.90}$ Fe $_{0.10}$ O nanoparticles which indicates that all the samples consist of Zn, O, or Fe, confirming that the incorporation of Fe into the samples. The EDXS analysis revealed that the nanoparticles with our selected ratios are nearly stoichiometric.

3.3 Microstructural characterization

Powder XRD of the pristine and Fe-doped ZnO nanostructure are described in Fig. 3. All samples of Zn $_{1-x}$ Fe $_x$ O ($x = 0, 0.04, 0.08, 0.10$ and 0.15) have a single hexagonal phase of ZnO and spacegroup “P6 $_3$ mc” according to open cryptography code # 00-900-4178. No contamination was detected, like Fe cluster or Fe $_2$ O $_3$, implying that the amount of iron is fewer than the solubility limits. Nevertheless, we cannot eliminate the possibility of improving clusters or precipitates of secondary amorphous phase small enough not to be detected by the XRD measurements. The diffraction peak of 15% Fe-doped ZnO ($2\theta = 34.305^\circ$) has shifted towards lower angles

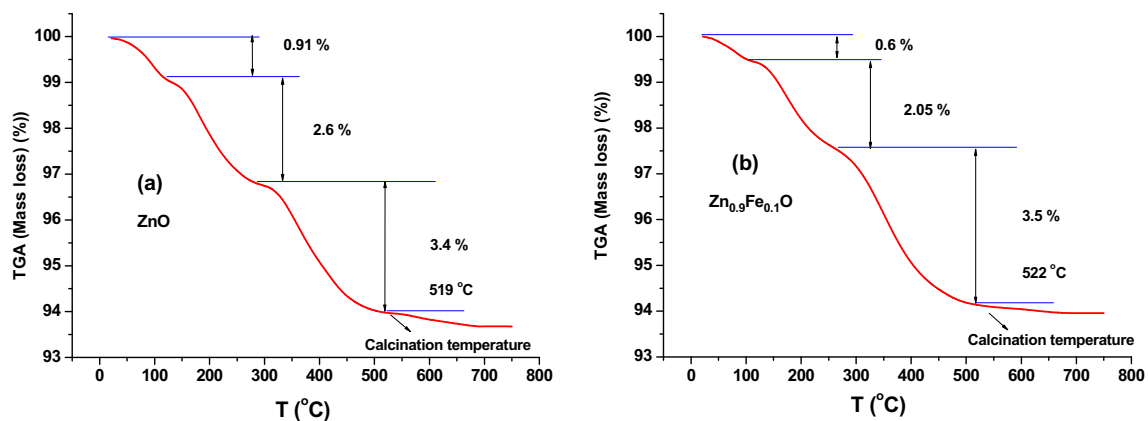


Fig. 1 a, b The TGA curves of pure and 10% Fe-doped ZnO nanoparticles

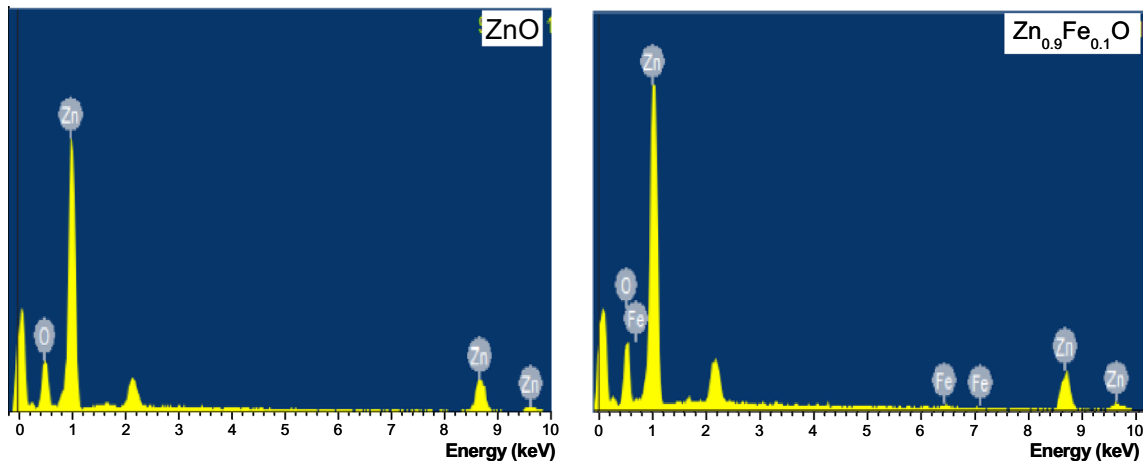


Fig. 2 The EDXS spectra for pure ZnO and Zn_{0.9}Fe_{0.1}O nanoparticles

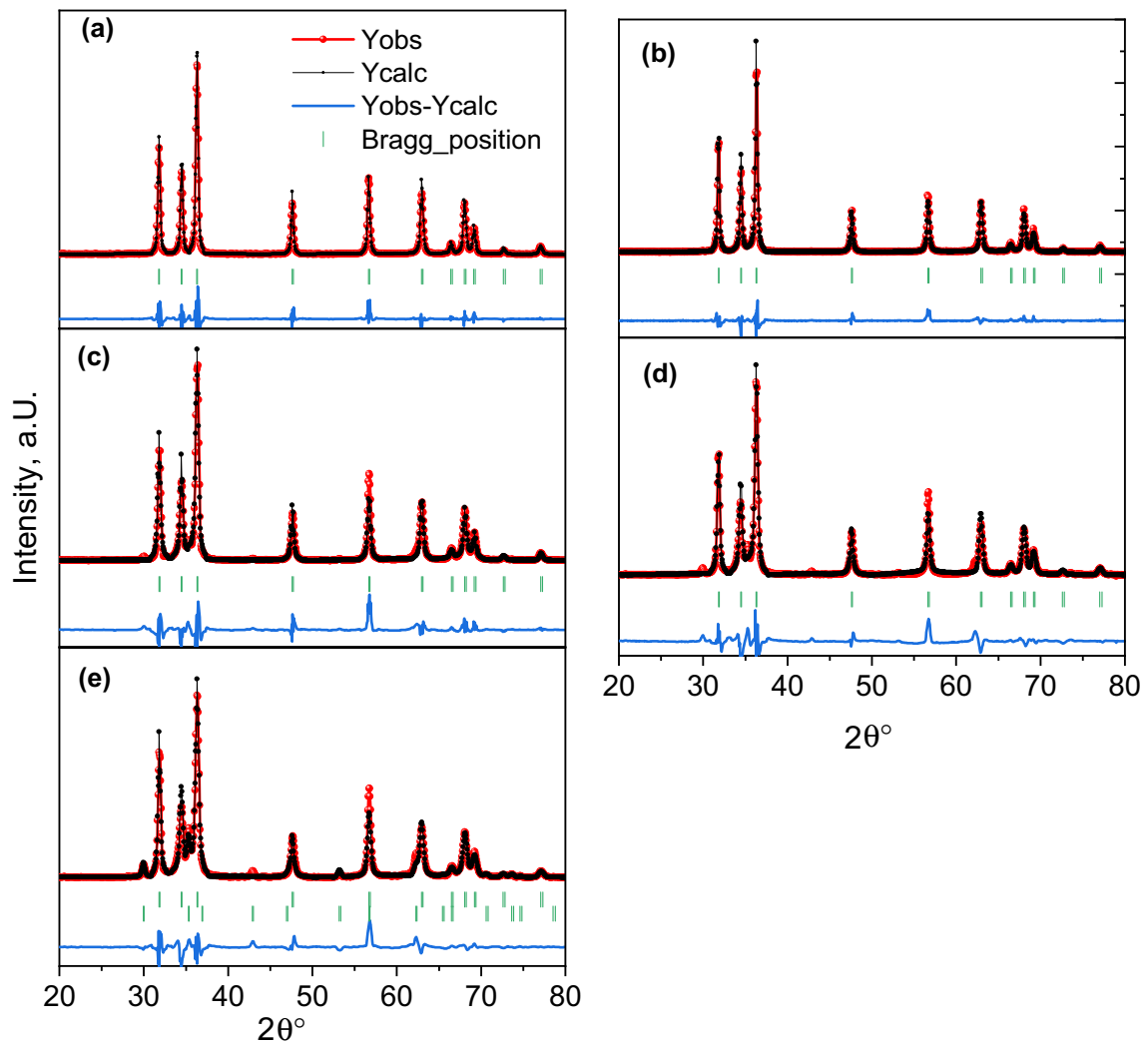


Fig. 3 a–e X-ray diffraction of Zn_{1-x}Fe_xO (x = 0, 0.04, 0.08, 0.10 and 0.15) nano-particle

compared to the pure ZnO ($2\theta = 34.355^\circ$), as exhibited in Fig. 3. This is because of the difference in ionic radii between Iron and Zinc that causes the existence of the tensile strain in the host (Zn) on the incorporation of the dopant ions into the basic cell of the powders. However, an increase in the concentration of Fe by more than 15% led to forming another phase from Fe_3O_4 . Formation in this phase may be referred to as the amount of iron that was not completely soluble in the Zn.

To more understand the impact of Fe ions on the lattice parameters of undoped ZnO, Rietveld refinement has been utilized. Rietveld-refined of the undoped and doped ZnO are exhibited in Fig. 3. Then, the lattice constants (a , c) have been computed systematically utilizing Rietveld refinement [15] employed in fullprof software. The obtained lattice parameter are plotted in Fig. 4.

By getting a diffraction pattern from the line broadening of standard material, it is possible to eliminate the instrumental broadening input using the following Eq. [16, 17]:

$$\beta_{hkl}(2\theta) = \sqrt{(\beta_{hkl})_{\text{measured}}^2 - (\beta_{hkl})_{\text{standard}}^2} \quad (1)$$

Here β_{hkl} is the (FWHM), β_c , and, β_s are defined in ref [19, 20]:

$$\beta_{hkl} = \beta_c + \beta_s = \frac{k\lambda}{D \cos \theta_0} + 4e(\sin \theta_0) \quad (2)$$

where D , k is the shape factor (≈ 0.9), and λ , and e are defined in the ref [17, 18].

The crystallite size was computed by applying Debye -Scherrer's formula [19, 20]

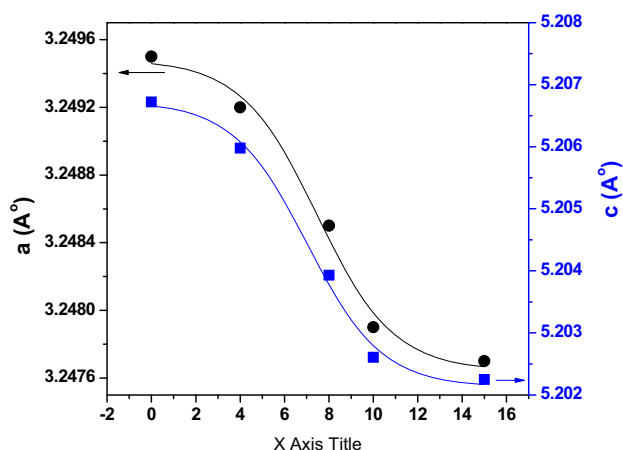


Fig. 4 Lattice parameters as a function of Fe content

$$D_v = \frac{k\lambda}{\beta \cos(\theta)} \quad (3)$$

where λ is the wavelength (1.54 Å).

The lattice strain (ε) parameter is estimated utilizing the following relation [19, 20]

$$\varepsilon = \frac{\beta}{4 \tan(\theta)} \quad (4)$$

The microstructural parameters s , e , and D_v for $\text{Zn}_{1-x}\text{Fe}_x\text{O}$ nanoparticles with several Fe contents are presented in Fig. 5. Clearly, the crystallite size reduces from 38 nm ($x = 0$) to 28 nm ($x = 0.15$) while the strain rises with increasing Fe substance. The variation of the crystallite size is strongly dependent only on preparation conditions and structure disorder[21]. During the preparation of the investigated samples, the preparation conditions were kept almost constant; accordingly, the grain size decreased due to the Fe ions being replaced by Zn ions.

3.4 XPS Studies

XPS examines the chemical composition of elements present in equipped samples. On all prepared samples, a comprehensive analysis was done. Figure 6a, b shows overview spectra of pristine and 10% Fe-doped ZnO nanoparticles synthesized by the precipitation route. From these figures, peaks associated with the elements Fe, Zn, O, and C are examined. To prove the coexistence of Fe^{2+} and Fe^{3+} ions in Fe-doped ZnO, we convoluted a 10% Fe spectrum, as

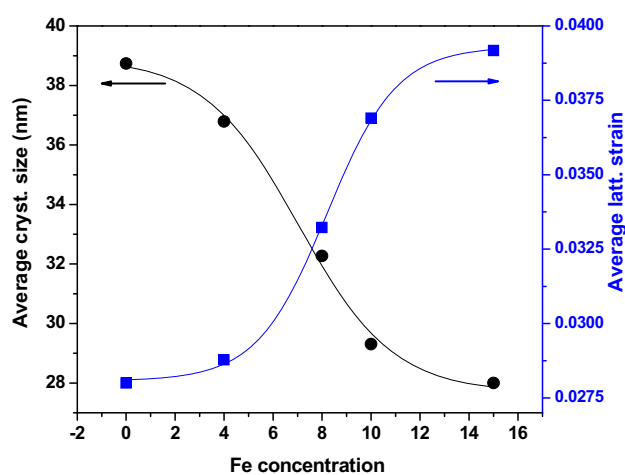


Fig. 5 Structural parameters as a function of Fe content

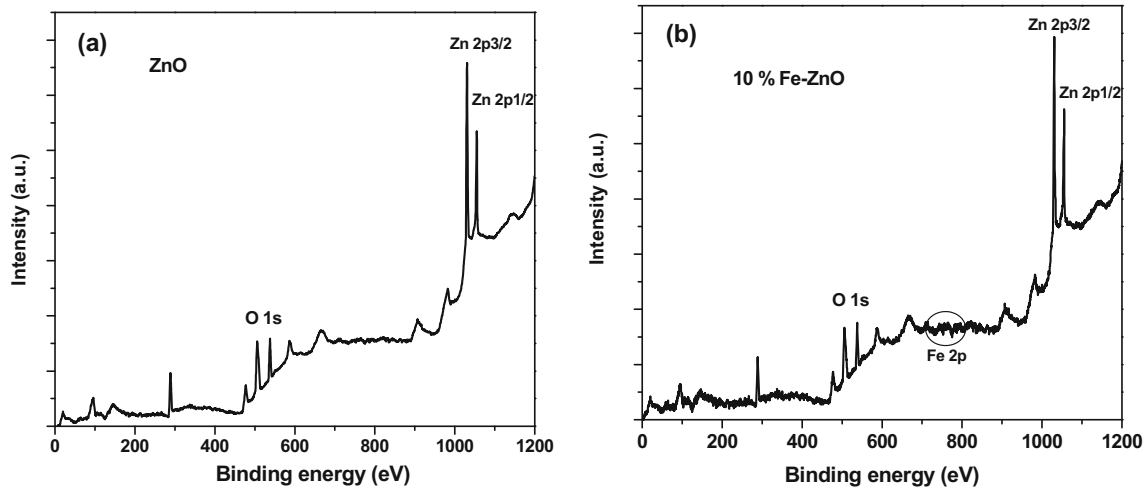


Fig. 6 XPS spectra for pure ZnO and Zn_{0.90}Fe_{0.10}O nanoparticles

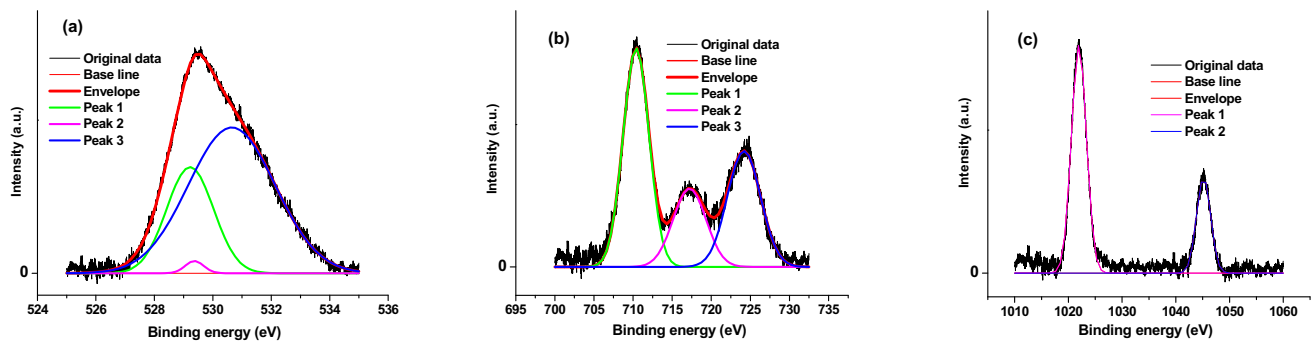


Fig. 7 Deconvolution of XPS spectrum peaks for Zn_{0.9}Fe_{0.10}O nanoparticles

presented in Fig. 7a–c). XPS central peak spectrum of O 1s for Fe-doped ZnO is revealed in Fig. 7b.

The XPS spectrum of the O 1s region shows asymmetric nature, demonstrating the attendance of different oxygen species. All peaks were deconvolved using a Gaussian fit. The nanoparticles synthesized by the precipitation method showed peaks at binding energies 529.27 eV, 529.5 eV, and 530.70 eV, as demonstrated in Fig. 7a, an O 1s peak is observed around 520.5 eV. It is owing to the O²⁻ bond with the metal, in our event Zn, which is Zn–O. The wide nature of the peaks may be owing to different oxygen coordinates in the samples. The peak at the lower binding energy centered at 529 eV is attributed to O ions surrounded by wurtzite-structured Zn atoms at tetrahedral sites. The higher binding energy peak centered at 530.7 eV is attributed to the oxygen vacancy defect.

It can be seen that Fe 2p_{3/2} and Fe 2p_{1/2} peaks and satellite peaks of the precipitation process are determined (Fig. 7b). It can be seen from the

figure that the Fe 2p_{3/2} and Fe 2p_{1/2} peaks of 10% Fe-doped nanoparticles synthesized by the precipitation method appear at 710.35 eV and 724.24 eV, respectively, with a peak spacing of 13.91 eV. The difference in binding energy originates from the coupling of spin–orbit between the atoms of Fe.

The binding energy of the Zn 2p peak was observed, as indicated in Fig. 7c. The binding energy of Zn 2p_{3/2} and 2p_{1/2} peaks are situated at 1021.50 eV and 1045.22 eV for 10% Fe-doped ZnO. This shows that zinc exists in 2+ states in all samples [22]

3.5 Optical characterization

Optical absorption measurements have an important task in investigating the behavior of semiconductor nanostructure. The energy band gap is considered to be the fundamental property of semiconductors. The absorbance of Zn_{1-x}Fe_xO ($x = 0, 0.04, 0.008, 0.10$ and 0.15) are presented in Fig. 8. The inset of this

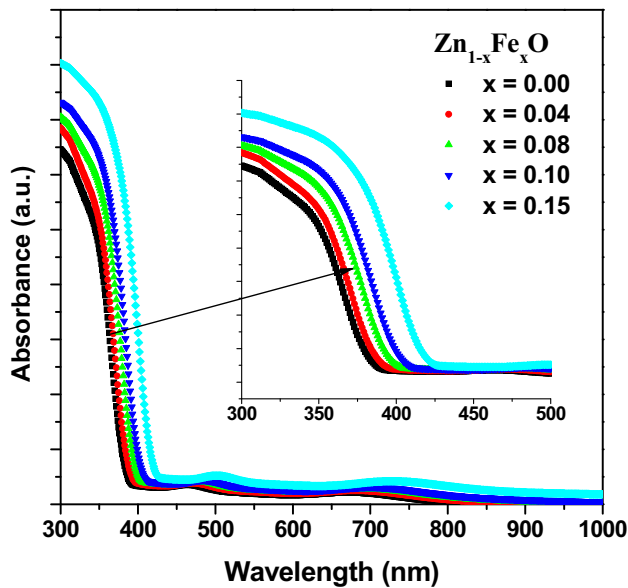


Fig. 8 Absorbance spectra of $Zn_{1-x}Fe_xO$ ($x = 0, 0.04, 0.08, 0.10$ and 0.15) nano-particles

figure shows an amplification the absorbance in the strong absorption region. To get the energy gap, E_g^{opt} value, the derivative of absorbance concerning wavelength was performed. Figure 10 illustrates the derivative absorbance of $Zn_{1-x}Fe_xO$ ($x = 0, 0.04, 0.08, 0.10$, and 0.15) nanoparticles as a function of wavelength. Figure 9 also shows the extent to which absorption increases with decreasing particle size (see Fig. 4). At larger particle sizes, the number of atoms required to build nanoparticles is huge, which

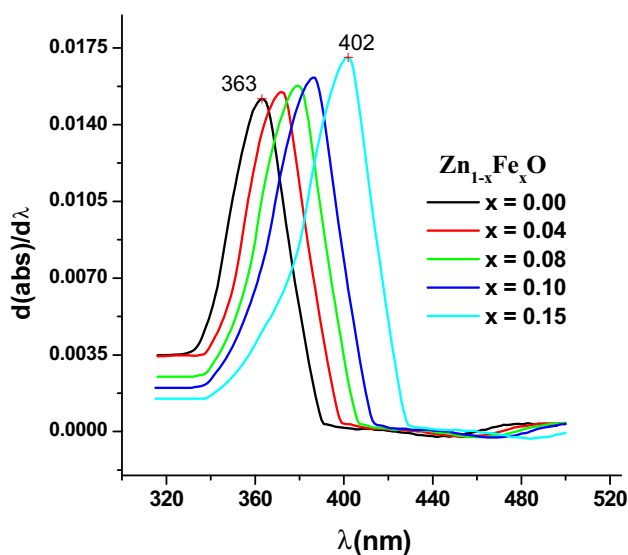


Fig. 9 Absorbance differentiation spectra of $Zn_{1-x}Fe_xO$ ($x = 0, 0.04, 0.08, 0.10$ and 0.15) nano-particles

increases the height of the maxima and the width of the peaks [22, 23]. The band energy of a nanoparticle can be determined from the location of the peak as $= hc/\lambda_{max}$. [24, 25] found that the energy gap of the investigated nanoparticles reduced from 3.41 eV ($x = 0$) to 3.1 eV (0.15) with rising Fe content.

It is observed that the absorption maximum λ_{max} red-shifts to longer wavelengths, from 363 to 402 nm, with rising Fe concentration in the semiconducting ZnO matrix due to reducing particle size. Figure 10 displays that the energy gap of $Zn_{1-x}Fe_xO$ reduces as the particle size decreases. This not only confirms the reduction of the energy gap, but also the reduction of the particle size with increasing Fe content. The transition to lower energies appears to be a low-dimensional quantum size effect due to electron and hole confinement in the semiconductor matrix. Therefore, the observed reduction in the energy gap of $Zn_{1-x}Fe_xO$ is due to the reduction in particle size, which is attributed to nanoscale electronic confinement, the so-called quantum confinement, or quantum size effect.

3.6 Photoluminescence (PL) studies

PL spectra of Fe-doped ZnO nanoparticles evaluated at RT employing a 325 nm wavelength excitation source are demonstrated in Fig. 11. Their peak separation (or deconvolute) spectra are shown in Fig. 12. PL peaks can be wide due to multiple recombination defects and sites. The PL asymmetric spectrum is attributed to the attendance of other peaks of an

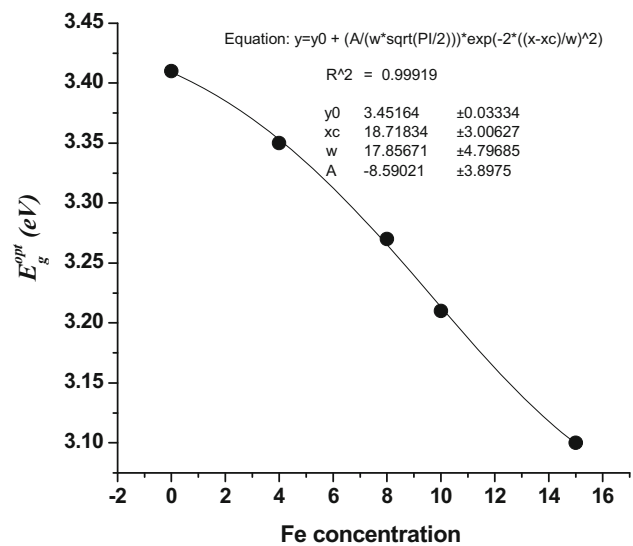


Fig. 10 Optical energy gap as a function of Fe content

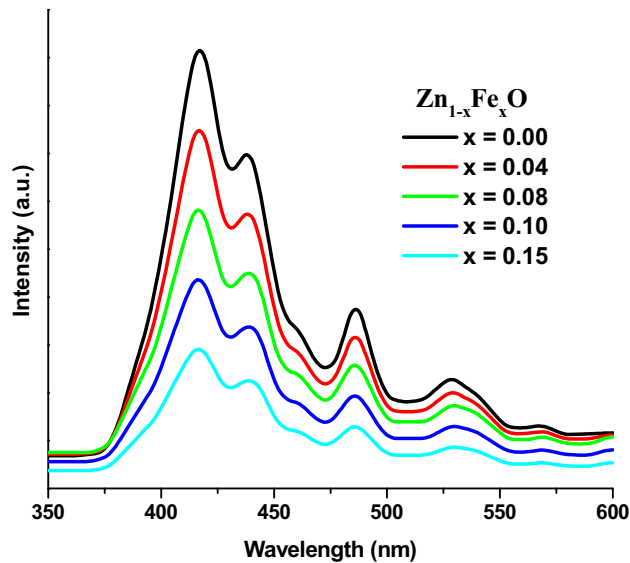


Fig. 11 PL spectra of $\text{Zn}_{1-x}\text{Fe}_x\text{O}$ ($x = 0, 0.04, 0.08, 0.10$ and 0.15) nano-particles

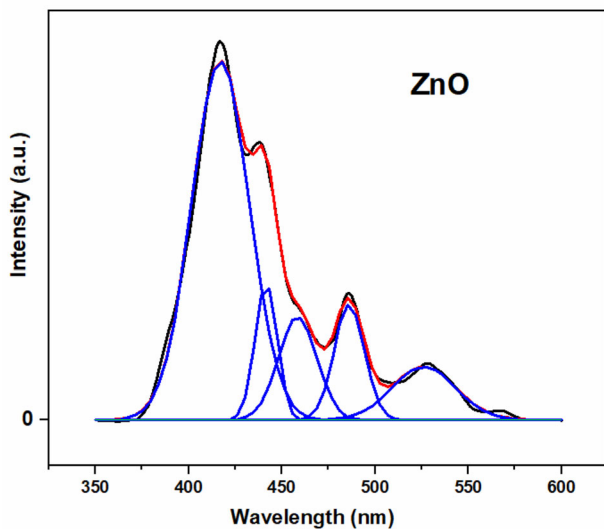


Fig. 12 Peaks separation of PL spectra for ZnO nanoparticle

intrinsic emission. These are produced by defect states that are spread on the outside and interior of a specific nanostructured system. This discovery contradicts a near-band-edge emission (NBE) peak in the (UV) region, whereas a (VL) emission peak is ascribed to DLD transitions. The UV emission band features an emission peak at 395 nm (3.12 eV), which is caused by excitonic recombination matching to the near-band edge emission of ZnO, according to Gaussian fitting of the PL spectra.

a lot of other visible emission bands adjusted to show at 422 nm (2.95 eV), 440 nm (2.83 eV), 465 nm

(2.67 eV), 489 nm (2.55 eV), 510 nm (2.44 eV) and 530 nm (2.34 eV). These fitted peaks correspond to the emissions of violet, blue and green. The broad and faint purple emission peak observed at 422 nm (2.95 eV) can be endorsed to the transition energy of electrons from conduction to interstitial oxygen (O_i). Furthermore, two faint broad peaks of the green emission were observed at 510 nm (2.44 eV) and 530 nm (2.34 eV) after the Gaussian fitting of the PL spectrum. The emission peak at 5010 nm may be due to the Zn_i to O_i transition, while the emission peak at 530 nm can be attributed to the conduction band OZn transition.

The blue emission is higher than the others. Their peaks at 440 nm (2.83 eV), 465 nm (2.67 eV), and 489 nm (2.55 eV) were cleared after Gaussian fitting of the PL spectra, which can be attributed to interstitial zinc (Zn_i) and oxygen-related defect. Correlation vacancy (V_o). Under the excitation of ultraviolet light, some photogenerated electrons can first decay to the defect energy level through a nonradiative transition process, and then transition to the valence band, in that way emitting blue light. Finally, the emission peak ~ 484 nm could be owing to impurities introduced during fabrication, which may attribute to inherent defects such as V_o to valence band transitions.

3.7 Magnetic characterization

To better understand the magnetic behavior of these Fe-doped ZnO nanoparticles with various concentrations (4%, 8%, 10%, and 15%), magnetization against field-dependent curves was determined at 300 K. Figure 13 exhibits pure ZnO diamagnetic performance, whereas Fe/ZnO nanoparticles reveal RTFM and magnetization rises with improving Fe substance. There was no indication of saturation in every sample. Based on the XRD and UV–Vis results, a possible clarification for the source of RTFM in Fe-doped ZnO nanoparticles can be originated. These results indicate that Fe^{2+} ions occupy Zn^{2+} sites within the lattice of the wurtzite ZnO crystal structure.

There is no evidence of secondary phase formation (metallic iron, iron oxide or zinc-iron binary phases) or clusters. These remarks propose that the magnetization is not owing to secondary phases or clusters. PL spectra obviously show that Fe doping induces multiple Zn_i and V_o defects. Consequently, it is

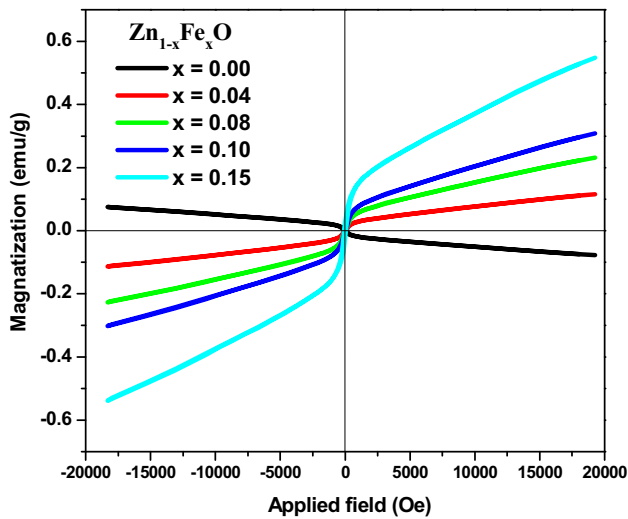


Fig. 13 M-H curve of $Zn_{1-x}Fe_xO$ ($x = 0, 0.04, 0.08, 0.10$ and 0.15) nano-particles

reasonable to assume that rich Zn_i and Vo defects may provide to RTFM by creating $Fe^{2+}-Fe^{2+}$ coupling in a ferromagnetic behavior. Therefore, only the exchange interactions among free delocalized charge carriers originating from oxygen vacancies and local d-spins on Fe ions are considered to be the source of ferromagnetism. It has been suggested that the relationship between defects and magnetism plays an important role in RT ferromagnetism.

The M-H plot of all Fe-doped ZnO nanoparticles demonstrates the creation of hysteresis loops, which means that the room temperature ferromagnetic behavior with a small coercive field and low remanence exhibits soft ferromagnetism. Several groups have reported that iron-doped ZnO nanoparticles are

ferromagnetic at and/or above room temperature [26, 27]. It has been proposed that the change in magnetization in Fe-doped ZnO is attributable to the shortening of the median distance among Fe ions with growing Fe content [28, 29]. Therefore, the weak magnetization observed at low Fe levels in this work can be attributed to the larger distance among iron ions, which weakens the ferromagnetic interaction.

Nevertheless, by adding the iron content, the ferromagnetic interaction becomes stronger (shorter iron ion spacing), thereby increasing the magnetization. Furthermore, the remanent magnetization (M_r) and coercive field (H_c) were estimated for all Fe-doped ZnO nanoparticles measured at room temperature. The coercivity rises as x increases from 59.9 G to 85.3 G ($x = 0.04$ to $x = 0.08$) (Fig. 14a) and M_r from 3.4×10^{-3} emu/g ($x = 0.02$) to 21×10^{-3} emu/g ($x = 0.15$) (Fig. 14b).

4 Conclusion

In conclusion, the structural and optical properties of pure ZnO and Fe-doped ZnO nanoparticles ($x = 0.04, 0.08, 0.10, \text{ and } 0.15$) produced by the precipitation process were studied. The patterns of XRD for all nanoparticles at different Fe concentrations showed wurtzite-type structures. The results show that the size of nanoparticles reduces from 39 nm (0%) to 28 nm (0.15%) with increasing Fe content, which is owing to the difference between the ionic radii of Zn and Fe. The optical absorption spectrum of the nanoparticles shows a red shift from 363 to 402 nm,

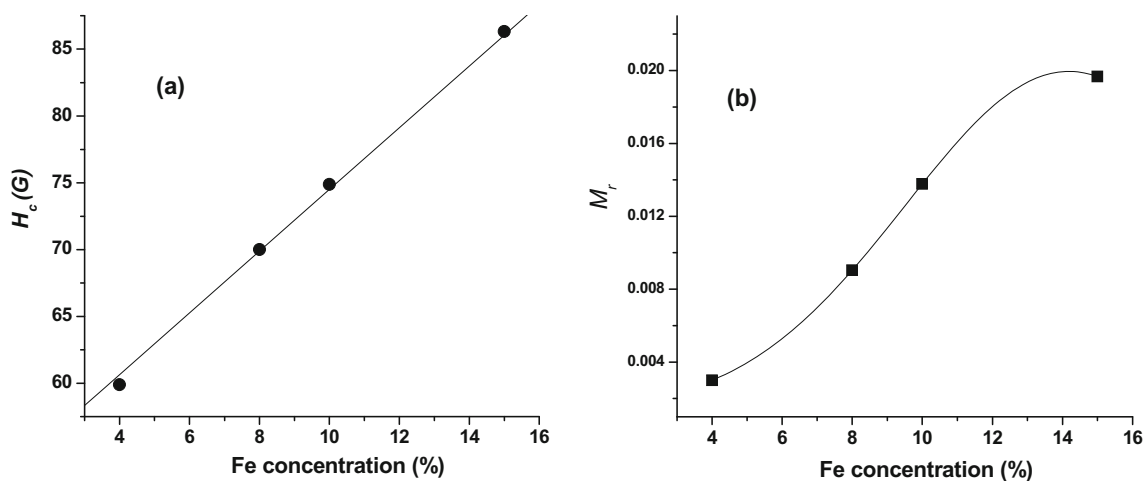


Fig. 14 H_c and M_r of $Zn_{1-x}Fe_xO$ as a function of Fe content

thus finding that the bandgap energy increases from 3.41 eV ($x = 0$) to 3.13 eV (0.15) with increasing Fe concentration due to particle reduction in size.

The light absorption and energy gap changes of ZnO nanoparticles can be controlled by Fe doping. XPS spectra of undoped and 10% Fe-doped ZnO nanoparticles synthesized by the precipitation process showed peaks associated with the elements to be observed Zn, O, Fe, and C. Verification of the coexistence of Fe^{2+} and Fe^{3+} ions in Fe-doped ZnO. Ferromagnetism is observed at RT for Fe-doped ZnO. The magnetization increases with the Fe content. These results suggest that Fe-doped ZnO is an excellent recommendation for the development of spintronic and optoelectronic devices.

Acknowledgements

The authors would like to express their gratitude to Princess Nourah bint Abdulrahman University Researchers Supporting Project (grant no. PNURSP 2022R32), Princess Nourah bint Abdulrahman University, Riyadh, Saudi Arabia. RSM: Conceptualization, Data curation, Writing—original draft. AAEl: Validation, Formal analysis. AAAS: Formal analysis, Writing—review & editing. BMA: review & editing, AA: review & editing, AMA: Investigation, Writing—review & editing. ERS: Supervision, Resources.

Funding

The authors have not disclosed any funding.

Data availability

The Data will be available when required from the corresponding author.

Declarations

Conflict of interest The authors have not disclosed any competing interests.

References

1. S.J. Pearton et al., ZnO doped with transition metal ions. *IEEE Trans. Electron Devices* **54**(5), 1040–1048 (2007)
2. A. Moezzi, A.M. McDonagh, M.B. Cortie, Zinc oxide particles: synthesis, properties and applications. *Chem. Eng. J.* **185**, 1–22 (2012)
3. D. Chu et al., Formation and photocatalytic application of ZnO nanotubes using aqueous solution. *Langmuir* **26**(4), 2811–2815 (2010)
4. J. Zhang et al., Hierarchically porous ZnO architectures for gas sensor application. *Cryst. Growth Des.* **9**(8), 3532–3537 (2009)
5. X.J. Liu et al., Intrinsic and extrinsic origins of room temperature ferromagnetism in Ni-doped ZnO films. *J. Phys. D Appl. Phys.* **42**(3), 035004 (2009)
6. J.R. Neal et al., Room-temperature magneto-optics of ferromagnetic transition-metal-doped ZnO thin films. *Phys. Rev. Lett.* **96**(19), 197208 (2006)
7. X. Huang et al., Morphology evolution and CL property of Ni-doped zinc oxide nanostructures with room-temperature ferromagnetism. *J. Phys. Chem. C* **113**(11), 4381–4385 (2009)
8. S. Benramache et al., Study on the correlation between crystallite size and optical gap energy of doped ZnO thin film. *J. Nanostruct. Chem.* **3**(1), 1–6 (2013)
9. Z.H. Zhang et al., Evidence of intrinsic ferromagnetism in individual dilute magnetic semiconducting nanostructures. *Nat. Nanotechnol.* **4**(8), 523–527 (2009)
10. N.H. Hong, J. Sakai, V. Brizé, Observation of ferromagnetism at room temperature in ZnO thin films. *J. Phys.: Condens. Matter* **19**(3), 036219 (2007)
11. R. Bhargava et al., Variation in structural, optical and magnetic properties of $\text{Zn}_{1-x}\text{Cr}_x\text{O}$ ($x = 0.0, 0.10, 0.15, \text{ and } 0.20$) nanoparticles: role of dopant concentration on non-saturation of magnetization. *Mater. Chem. Phys.* **125**(3), 664–671 (2011)
12. F.A. Taher, E. Abdeltwab, Shape-controlled synthesis of nanostructured Co-doped ZnO thin films and their magnetic properties. *CrystEngComm* **20**(38), 5844–5856 (2018)
13. A.K. Mishra, D. Das, Investigation on Fe-doped ZnO nanostructures prepared by a chemical route. *Mater. Sci. Eng. B* **171**(1–3), 5–10 (2010)
14. X.X. Wei et al., Local Fe structure and ferromagnetism in Fe-doped ZnO films. *J. Phys.: Condens. Matter* **18**(31), 7471 (2006)
15. A. Hewat, W.I.F. David, L. van Eijck, Hugo Rietveld (1932–2016). *J. Appl. Crystallog.* **49**(4), 1394–1395 (2016)
16. A.F. Al Naim, A. Solieman, E.R. Shaaban, Structural, optical, and magnetic properties of Co-doped ZnO nanocrystalline thin films for spintronic devices. *J. Mater. Sci.: Mater. Electron.* **31**(4), 3613–3621 (2020)
17. A.C. Galca, G. Socol, V. Craciun, Optical properties of amorphous-like indium zinc oxide and indium gallium zinc

- oxide thin films. *Thin Solid Films* **520**(14), 4722–4725 (2012)
18. P.-Y. Kim et al., Structure and properties of IZO transparent conducting thin films deposited by PLD method. *J. Korean Phys. Soc.* **53**(1), 207–211 (2008)
 19. B.D. Cullity, *Elements of X-ray diffraction*, 2nd edn. (Addition-Weasley, London, 1978)
 20. J.I. Langford, A.J.C. Wilson, *J. Appl. Cryst.* **11**, 102–113 (1978)
 21. M. Ghosh et al., Metal-ion displacement approach for optical recognition of thorium: application of a molybdenum (VI) complex for nanomolar determination and enrichment of Th (IV). *ACS Omega* **3**(11), 16089–16098 (2018)
 22. T. Srinivasulu, K. Saritha, K.T.R. Reddy, Synthesis and characterization of Fe-doped ZnO thin films deposited by chemical spray pyrolysis. *Mod. Electron. Mater.* **3**(2), 76–85 (2017)
 23. X. Gong et al., Engineering high-emissive silicon-doped carbon nanodots towards efficient large-area luminescent solar concentrators. *Nano Energy* **101**, 107617 (2022)
 24. M. El-Hagary et al., The particle size-dependent optical band gap and magnetic properties of Fe-doped CeO₂ nanoparticles. *Solid State Sci.* **91**, 15–22 (2019)
 25. T.A. Abdel-Baset et al., Structural and magnetic properties of transition-metal-doped Zn_{1-x}Fe_xO. *Nanoscale Res. Lett.* **11**(1), 1–12 (2016)
 26. A. Popa et al., Interplay between ferromagnetism and photocatalytic activity generated by Fe³⁺ ions in iron doped ZnO nanoparticles grown on MWCNTs. *Physica E: Low Dimens. Syst. Nanostruct.* **129**, 114581 (2021)
 27. J.J. Beltrán, C.A. Barrero, A. Punnoose, Understanding the role of iron in the magnetism of Fe doped ZnO nanoparticles. *Phys. Chem. Chem. Phys.* **17**(23), 15284–15296 (2015)
 28. M. Zahan, J. Podder, Role of Fe doping on structural and electrical properties of MnO₂ nanostructured thin films for glucose sensing performance. *Mater. Sci. Semicond. Process.* **117**, 105109 (2020)
 29. M.M. Ovhal et al., Photoluminescence quenching and enhanced spin relaxation in Fe doped ZnO nanoparticles. *Mater. Chem. Phys.* **195**, 58–66 (2017)

Publisher's Note Springer Nature remains neutral with regard to jurisdictional claims in published maps and institutional affiliations.

Springer Nature or its licensor holds exclusive rights to this article under a publishing agreement with the author(s) or other rightsholder(s); author self-archiving of the accepted manuscript version of this article is solely governed by the terms of such publishing agreement and applicable law.